Nanoscale

PAPER

View Article Online
View Journal | View Issue



Cite this: *Nanoscale*, 2025, **17**, 19169

# Bioactive herbal supramolecular hydrogels with a hierarchical nanofibrillar structure *via* metal ion mediated co-assembly†

Xinke Yu,[a] Sili Liu,[a] Zhili Wan *[a,b] and Xiaoquan Yang [a]

Supramolecular hydrogels assembled from natural herbal small molecules represent a promising platform for the development of biocompatible and multifunctional soft biomaterials. In this study, we report a novel multicomponent supramolecular hydrogel system constructed from the co-assembly of glycyrrhizic acid (GA) and rhein (Rh) *via* $Zn^{2+}$ modulation. The introduction of $Zn^{2+}$ not only reinforces the mechanical stiffness and toughness of the GA–Rh hydrogel network through complexation but also improves its antibacterial efficacy and anti-inflammatory capacity. Notably, a hierarchical nanofibrillar gel network with an internal multiscale structure is formed, in which a micron-scale pore network formed by the GA nanofibrils and a submicron-scale pore network formed by the GA–Rh co-assembled nanofibrils synergistically contributed to the overall structural integrity and biological performance. *In vitro* assays demonstrate that the GA–Zn–Rh hydrogels exhibit potent antibacterial activity against *Staphylococcus aureus* and *Escherichia coli*, excellent biocompatibility, and pronounced anti-inflammatory effects. This work provides valuable insights into the relationships between nanostructure and functionality in multicomponent bioactive herbal hydrogels, offering a supramolecular strategy to mimic the synergistic therapeutic principles of traditional Chinese medicine. These findings pave the way for the development of nature-inspired bioactive hydrogels for wound healing and broader biomedical applications.

Received 16th May 2025,
Accepted 22nd July 2025

DOI: 10.1039/d5nr02063h

rsc.li/nanoscale



## 1. Introduction

Supramolecular hydrogels, typically constructed through the self-assembly of low molecular weight gelators (LMWGs) *via* non-covalent interactions, have emerged as a class of versatile and dynamic functional soft materials.[1–6] In recent years, supramolecular hydrogels formed from natural herbal-derived LMWGs have attracted considerable attention owing to their excellent biocompatibility, intrinsic biological activities, and environmentally friendly fabrication processes.[7–11] To achieve precise control over the hierarchical structures and synergistic therapeutic functionalities of these natural systems, increasing efforts have focused on the co-assembly of multiple herbal-derived LMWGs, enabling the creation of multicomponent supramolecular hydrogels with tunable architectures and diverse biomedical applications, such as wound healing and drug delivery.[12–17] Drawing inspiration from the macroscopic therapeutic principle of traditional Chinese medicines, which emphasizes the combination of multiple natural components to achieve synergistic effects, it is desirable to explore how distinct herbal LMWGs interact, co-assemble into hierarchical nanostructures, and collectively modulate biological activities. Therefore, there is a need to imitate the cooperative therapeutic strategies of traditional Chinese medicines at the supramolecular level by elucidating the intrinsic relationships between nanostructures and biofunctionality in these multicomponent systems, which can advance the rational design of nature-inspired, multifunctional bioactive hydrogels for biomedical applications.

Among these natural herbal small molecules, glycyrrhizic acid (GA), a naturally occurring amphiphilic triterpenoid saponin extracted from licorice root, exhibits a range of biological activities, including anti-inflammatory, hepatoprotective, anticancer, and antiviral properties.[18–20] Structurally, GA is a chiral amphiphilic molecule comprising a hydrophobic triterpenoid aglycone (18β-glycyrrhetinic acid) linked to a hydrophilic diglucuronic acid moiety. This inherent amphiphilic and chiral character enables GA molecules to undergo anisotropic self-assembly to form supramolecular nanofibrils in aqueous environments, driven by hydrophobic interactions among the triterpenoid segments and hydrogen bonding

[a]*Laboratory of Food Proteins and Colloids, School of Food Science and Engineering, Guangdong Province Key Laboratory for Green Processing of Natural Products and Product Safety, South China University of Technology, Guangzhou 510640, China. E-mail: zhiliwan@scut.edu.cn*

[b]*Overseas Expertise Introduction Center for Discipline Innovation of Food Nutrition and Human Health (111 Center), Guangzhou 510640, China*

† Electronic supplementary information (ESI) available. See DOI: https://doi.org/10.1039/d5nr02063h

between the glucuronic acid residues.[21,22] The resulting semi-flexible nanofibrils exhibit a right-handed helical twist, with a width of approximately 2.5 nm and a periodicity of 9 nm, which subsequently entangle to form supramolecular hydrogels featuring three-dimensional networks.[23] Moreover, the abundance of functional groups, rigid molecular backbone, and distinctive stacking behavior endow GA with exceptional structural versatility, facilitating the synthesis of a broad spectrum of GA derivatives and advancing the development of multifunctional hydrogel materials.[24–26] Harnessing this unique combination of intrinsic bioactivities and self-assembly capabilities, we have successfully fabricated versatile GA-based supramolecular hydrogels with favorable mechanical properties, stimuli-responsive behavior, and multifunctionality, demonstrating the promising potential in biomedical applications such as controlled drug delivery and wound healing.[27–30] Rhein (Rh), an anthraquinone compound primarily isolated from the traditional Chinese medicinal herb *Rheum palmatum*, is another bioactive herbal molecule with notable neuroprotective, anti-inflammatory, and antibacterial activities.[31–33] Notably, Rh possesses the intrinsic ability to self-assemble into supramolecular hydrogels *via* intermolecular π–π stacking and hydrogen bonding interactions.[31] Combining GA and Rh may offer the potential to create supramolecular hydrogels with complementary biological functionalities and novel nanostructures by employing the multicomponent co-assembly approach. In addition, the mechanical weakness of GA-based supramolecular hydrogels, especially those assembled from small molecules alone, often limits their practical applications.

To address the issue of unsatisfactory mechanical and functional properties, our previous study has demonstrated that $Zn^{2+}$ possesses a strong complexation capability with GA, markedly improving the mechanical properties of the GA hydrogels and also promoting intrinsic antibacterial properties.[34] It is known that metal ions such as $Zn^{2+}$ can modulate the supramolecular assembly process by altering intermolecular interactions and electrostatic environments, thereby regulating the nanostructural organization and enhancing the biological functionalities of hydrogels.[35] Therefore, we hypothesize that $Zn^{2+}$ could also tune the co-assembly behavior of GA and Rh, thereby tuning both the structural and functional properties of the resulting multicomponent hydrogels. Herein, by employing $Zn^{2+}$ as a modulating agent, we successfully prepared GA–Zn–Rh co-assembled supramolecular hydrogels with excellent mechanical robustness and desirable biological performance (Scheme 1). The hierarchical nanofibrillar architectures and network features of these hydrogels were systematically visualized *via* cryo-scanning electron microscopy (Cryo-SEM) and atomic force microscopy (AFM). Notably, a hierarchical gel network with an internal multiscale structure was identified, wherein GA nanofibrils first formed a micron-scale porous network, followed by the formation of a submicron-scale porous network through the co-assembly of GA and Rh, together constituting an interpenetrating supramolecular nanofibrillar network. The underlying assembly mechanism governing the formation of this hierarchical gel network was comprehensively investigated through isothermal titration calorimetry (ITC), zeta potential analysis, and a series of spectroscopic techniques. The antibacterial, biocompatibility, and anti-inflammatory properties of the GA–Zn–Rh hydrogels were thoroughly evaluated *via in vitro* antibacterial assays against *Staphylococcus aureus* (*S. aureus*) and *Escherichia coli* (*E. coli*), cytocompatibility assessments using L929 fibroblasts and RAW264.7 macrophages, and *in vitro* anti-inflammatory tests, respectively. This work represents the first demonstration of the multicomponent supramolecular hydrogels derived entirely from all-natural herbal small molecules, GA and Rh, assembled *via* metal ion-mediated complexation. Importantly, this work highlights the role of hierarchical structures and multicomponent assemblies in enhancing the functional performance of herbal supramolecular hydrogels, showing a great potential for biomedical use.

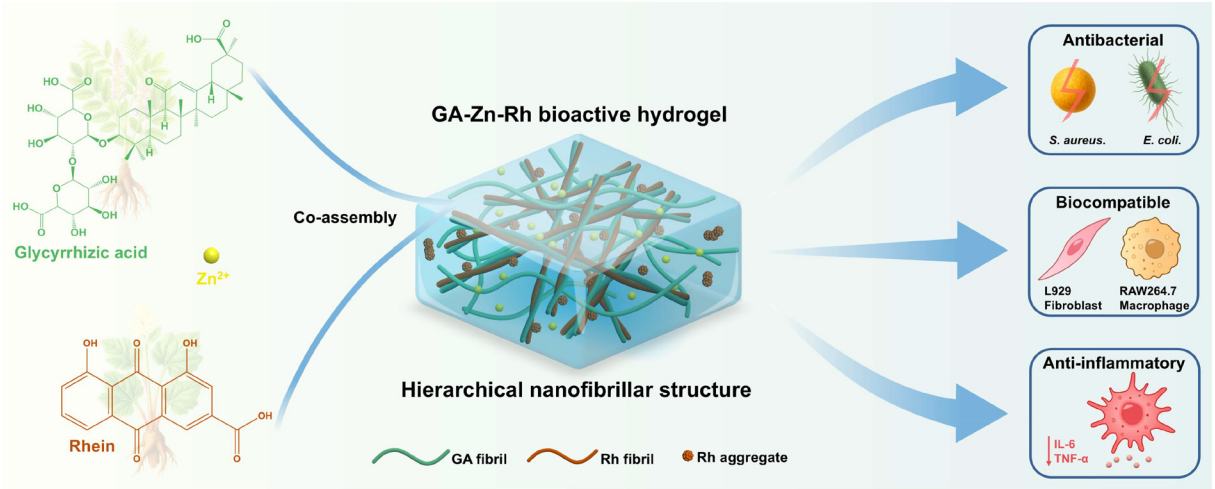


**Scheme 1** Schematic illustration of GA–Zn–Rh co-assembled bioactive herbal supramolecular hydrogels.

# 2. Experimental

## 2.1 Materials

Glycyrrhizic acid mono ammonium salt (GA, purity >98%) was purchased from Thermo Fisher, (USA). Rhein (Rh) was purchased from Shanghai Aladdin Co., Ltd (China). *S. aureus* (ATCC29213) and *E. coli* (ATCC8739) were obtained from the National Institutes for Food and Drug Control. L929 fibroblasts and RAW264.7 macrophages were purchased from the Cell Bank of the Chinese Academy of Sciences. High-sugar Dulbecco's modified Eagle's medium (DMEM), modified Eagle's medium (MEM) and Dulbecco's phosphate-buffered saline (DPBS) were purchased from Gibco Biotechnology (USA). 3-(4,5-Dimethylthiazol-2)-2,5-diphenyltetrazolium bromide (MTT), dimethyl sulfoxide (DMSO), and lipopolysaccharide (LPS) (L2880) were purchased from Sigma-Aldrich (USA). Fetal bovine serum, horse serum, TrypLE Express enzyme, 1× penicillin–streptomycin–glutamine, mouse interleukin 6 (IL-6) and mouse tumor necrosis factor α (TNF-α) enzyme-linked immunosorbent assay (ELISA) kits were purchased from Thermo Fisher Scientific (USA). Calcein/PI cell activity and cytotoxicity assay kit was purchased from Shanghai Biyuntian Biotechnology Co. Milli-Q water (18.2 MΩ cm) was used in this work, and all chemicals used were of analytical grade.

## 2.2 Preparation of GA–Zn–Rh hydrogels

Stock solution of GA (8 wt%) was prepared by dissolving GA powder in water and heating at 80 °C under mild agitation to obtain a transparent solution. Stock solution of Rh (2 wt%) was obtained by first dissolving Rh powder in water, followed by sonication to promote dissolution. The mixture was then heated at 80 °C under mild agitation to obtain a homogeneous solution. $ZnCl_2$ solution (2 M) was prepared by dissolving $ZnCl_2$ powder in water and adjusting pH to 4.0 to prevent hydrolysis. Subsequently, the GA, Rh, and $ZnCl_2$ solutions were mixed in different volume ratios at 80 °C to acquire the desired sample concentration. The resulting samples were stored overnight (12 h) at room temperature (25 °C) before further use. The final concentrations of GA and Rh were 2 wt% and 0.25–1 wt%, respectively, and the concentration of $Zn^{2+}$ was 10 mM. The corresponding hydrogels were termed GA, GA–Zn, GA–$Rh_x$, and GA–Zn–$Rh_x$ ($x$ represents the concentration of Rh). The gelation of the sample was determined by the tube inverted test, and the gel formation was verified if no visual fluidity was observed after 1 min of tube inversion.

## 2.3 Cryo scanning electron microscopy (Cryo-SEM)

The hydrogel samples were fixed on a holder and snap-frozen with liquid nitrogen slush before being transferred into a cryo chamber (PP3010T, Quorom, UK) at −140 °C. The samples were afterward sublimated for 30 min at −90 °C to remove frost artifacts. Finally, the samples were scanned with a scanning electron microscope (S-4800, Hitachi) at 3 kV.

## 2.4 Field emission scanning electron microscopy (FE-SEM)

The microstructures of freeze-dried hydrogel samples were observed on a Zeiss Merlin field emission scanning electron microscope (Zeiss, Germany). The samples were carefully transferred and firmly attached to a holder, and then sputter-coated with gold (JEOL JFC-1200 fine coater, Japan) before imaging at 5 kV.

## 2.5 Atomic force microscopy (AFM)

A droplet of hot hydrogel sample was deposited on freshly cleaved mica and dried on air. AFM measurements were performed by using a Bruker Dimension Icon atomic force microscopy (Bruker, Germany) in tapping mode. AFM images were analyzed using NanoScope Analysis software.

## 2.6 Isothermal titration calorimetry (ITC)

Thermodynamics of the binding between GA and $Zn^{2+}$, GA and Rh were investigated by isothermal titration calorimeter (Malvern Instruments Ltd USA). All experiments were conducted at 25 °C with 60 μL of $ZnCl_2$ or Rh solution (40 mM) titrated into 300 μL of GA solution (2 mM) in the sample cell. Accordingly, $ZnCl_2$ or Rh solution titrated into water was used as blank control. The heat of dilution from the blank titration of titrants into water was subtracted from the raw data. The reference cell, which was housed with the sample cell in an adiabatic chamber, consisted of water. Each individual injection lasted 4 s, and the time interval between injections was 150 s. Data was analysed by MicroCal PEAQ-ITC software and titration curves were fitted by one set of sites fitting model. Thermodynamic parameters, including the association constant ($K_a$), dissociation constant ($K_d$), Gibbs free energy change ($\Delta G$), enthalpy change ($\Delta H$), and entropy change ($\Delta S$), were calculated by iterative curve fitting of the binding isotherms using following equation:

$$Q = \frac{(1 + [\mathrm{M}]_t \cdot n \cdot K_a + K_a \cdot [\mathrm{L}]_t) - \sqrt{\left[(1 + [\mathrm{M}]_t \cdot n \cdot K_a + K_a \cdot [\mathrm{L}]_t)^2 - 4 \cdot [\mathrm{M}]_t \cdot n \cdot K_a{}^2 \cdot [\mathrm{L}]_t\right]}}{2 \cdot K_a / V \cdot \Delta H} \quad (1)$$

$$\Delta G = -RT \ln K_a = \Delta H - T\Delta S \quad (2)$$

$$K_d = \frac{1}{K_a} \quad (3)$$

where $Q$ is the cumulative heat, $[\mathrm{M}]_t$ is the total concentration of reactants in the sample cell, $[\mathrm{L}]_t$ is the total concentration of titrant added, $V$ is the volume of the sample cell, $R$ is the gas constant (8.314 $\mathrm{Jmol^{-1}\,K^{-1}}$), and $T$ is the absolute temperature (in kelvin).

### 2.7 Fourier transform infrared spectroscopy (FTIR)

FTIR spectra of freeze-dried hydrogel samples were recorded at 400–4000 $cm^{-1}$ using an FTIR spectrophotometer (Thermo Fisher, USA) equipped with a narrow-band mercury cadmium telluride detector with a resolution of 2 $cm^{-1}$.

### 2.8 X-ray photoelectron spectroscopy (XPS)

XPS measurements were performed using a Kratos Axis Supra$^+$ XPS instrument (Kratos, UK). Al Kα radiation was used, and the chamber pressure was less than $5 \times 10^{-9}$ torr during operation. The XPS spectra were scanned with the pass energy of 160 eV and 40 eV for full and narrow spectra, respectively. Thermo Scientific Avantage software was used for data analysis. The data was calibrated based on the C 1s peak at 284.8 eV, and a smart-type background was used.

### 2.9 $^1$H nuclear magnetic resonance ($^1$H-NMR)

The structure composition of complex units was elucidated by Avance IIIHD 600 MHz spectrometer (Bruker, Germany).

### 2.10 Ultraviolet-visible spectroscopy

The hydrogel samples were diluted 20 times and transferred to10 mm quartz cuvettes (200–900 nm) at a test temperature of 25 °C. The UV-vis absorption spectrum (200–900 nm) was then acquired using a C40 Touch UV-Vis spectrophotometer (Implen, Germany).

### 2.11 *In vitro* antibacterial activity

In the antibacterial assay, *Staphylococcus aureus* (*S. aureus*) and *Escherichia coli* (*E. coli*) were selected as representative Gram-positive and Gram-negative bacterial strains, respectively. Hydrogels were prepared under aseptic conditions following the aforementioned protocols. Briefly, bacterial stock suspensions of *S. aureus* and *E. coli* were inoculated into 20 mL of Luria–Bertani (LB) medium and incubated at 37 °C for 12 h with continuous shaking at 100 rpm. The resulting cultures were centrifuged at 5000 rpm for 10 min, and the supernatants were discarded. The bacterial pellets were then resuspended in sterile PBS (pH 7.4) and adjusted to an optical density ($OD_{600}$) of approximately 0.65. For real-time monitoring of bacterial growth kinetics, the bacterial suspensions ($OD_{600} \approx 0.65$) were further diluted 1 : 100 in fresh LB medium. Aliquots of the diluted bacterial suspension (30 mL) were supplemented with 3 g of hydrogel or an equivalent volume of PBS and incubated at 37 °C with shaking at 100 rpm. The optical density at 600 nm ($OD_{600}$) was recorded at predefined time intervals throughout the incubation period. For colony-forming unit (CFU) enumeration, 10 μL of bacterial suspension ($OD_{600} \approx 0.65$) was dispensed onto the surface of 0.2 g of hydrogel and incubated at 37 °C for 2 h. Subsequently, 990 μL of sterile PBS was added to the resuspend bacterial survivors. In parallel, a control group was prepared by adding 10 μL of bacterial suspension to 0.2 g of PBS solution under identical conditions. Following incubation, the suspensions were serially diluted $10^2$–$10^6$ fold with sterile PBS, and 50 μL of each dilution was spread onto LB agar plates. The plates were incubated at 37 °C for 24 h prior to CFU enumeration. All experiments were performed in triplicate. The survival rate of bacteria was calculated by the following equation:

$$\text{Survival rate}\,(\%) = \frac{\text{CFU count}\,(\text{hydrogel} - \text{treated group})}{\text{CFU count}\,(\text{control group})} \times 100 \quad (4)$$

For further morphological characterization of the bacteria, samples were collected and fixed in 2.5% (v/v) glutaraldehyde solution for 4 h at 25 °C. The fixed specimens were subsequently dehydrated through a graded ethanol series, and the morphologies of bacteria were observed by FE-SEM.

### 2.12 *In vitro* cytocompatibility

Mouse fibroblast cells (L929) and mouse mononuclear macrophages leukemia cells (RAW264.7) were employed to assess the cytocompatibility of GA–Rh–Zn hydrogels. Biocompatibility was evaluated *via* a material extract method coupled with MTT reduction assays. For cytotoxicity analysis in L929 cells, hydrogel extract liquids were prepared by immersing 0.1 g of hydrogel in 5 mL of modified Eagle's medium (MEM) and incubating at 37 °C under 5% $CO_2$ for 24 h. L929 cells were maintained in MEM supplemented with 10% donor equine serum in a humidified atmosphere containing 5% $CO_2$ at 37 °C. Cells were seeded into 96-well plates at a density of $1 \times 10^4$ cells per well and incubated for 24 h under standard culture conditions. Subsequently, the culture medium was replaced with fresh medium containing varying concentrations of hydrogel extract liquids (0.2, 1, and 5 mg $mL^{-1}$). Following a 24 h incubation with the extract liquids, the media were substituted with MTT solution (0.5 mg $mL^{-1}$) and incubated for an additional 4 h at 37 °C in 5% $CO_2$. The absorbance was then measured at 570 nm using a microplate reader. Cells treated with PBS served as the control. The cell viability was calculated by the following equation:

$$\text{Cell viability}\,(\%) = \frac{A_{\text{test}} - A_{\text{blank}}}{A_{\text{control}} - A_{\text{blank}}} \times 100 \quad (5)$$

where $A_{\text{test}}$ represents the absorbance of hydrogel groups; $A_{\text{blank}}$ represents the absorbance of pure MTT solution without cells; and $A_{\text{control}}$ represents the absorbance of the control group. Live/dead fluorescence staining was conducted to evaluate cell toxicity following a 24 h incubation with hydrogel extract liquids (5 mg $mL^{-1}$). Viable cells were labeled with calcein-AM, emitting green fluorescence, while non-viable cells were stained with propidium iodide (PI), yielding red fluorescence. The cytocompatibility of the hydrogels towards RAW264.7 cells was assessed using an identical protocol to that employed for L929 cells. Specifically, RAW264.7 cells were cultured in Dulbecco's modified Eagle's medium (DMEM) supplemented with 10% fetal bovine serum.

 

### 2.13 *In vitro* anti-inflammatory assays

The *in vitro* anti-inflammatory properties of the hydrogels were assessed using a lipopolysaccharide (LPS)-induced inflammatory model. Briefly, RAW 264.7 macrophages were cultured in complete medium under standard conditions (37 °C, 5% $CO_2$) for 24 h, and subsequently seeded into 12-well plates at a density of $1 \times 10^5$ cells per well. To induce an inflammatory response, cells were stimulated with LPS (1 mL, 300 ng $mL^{-1}$) for 24 h. Following stimulation, 1 mL of medium containing hydrogel extract liquids was added to each well, and the cultures were maintained for an additional 24 h. The concentrations of pro-inflammatory cytokines, including interleukin-6 (IL-6) and tumor necrosis factor-α (TNF-α) in the collected supernatants were quantified using enzyme-linked immunosorbent assay (ELISA) kits.

### 2.14 Statistical analysis

All testing was performed in triplicate unless specifically mentioned and results were presented as mean ± standard deviation for all measurements. The statistical differences between groups were tested by one-way analysis of variance (ANOVA) for multiple comparisons followed by LSD's *post hoc* test using the OriginPro 2021 software. *P*-Value < 0.05 was considered statistically significant ($*p < 0.05$, $**p < 0.01$, $***p < 0.001$).

## 3 Results and discussion

### 3.1 Preparation and characterization of GA–Zn–Rh hydrogels

The supramolecular fibrillar self-assembly and intrinsic biological activities of GA molecules endow them with significant potential as multifunctional building blocks for the design of natural bioactive hydrogels. Nevertheless, the inherently weak mechanical strength and limited processability of pure GA hydrogels pose substantial constraints on their practical utility in food and biomedical applications. To address these limitations, we strategically employed $Zn^{2+}$ to modulate the self-assembly behaviors of two natural LMWGs, GA and Rh. Based on the multicomponent co-assembly strategy, we successfully fabricated GA–Zn–Rh co-assembled supramolecular hydrogels featuring hierarchical nanofibrillar architectures, significantly improved mechanical performance, and enhanced biological functionalities. The hydrogels were prepared *via* a straightforward one-pot method, wherein GA, ultrasonicated Rh, and $ZnCl_2$ solutions were combined under continuous stirring and heating, followed by cooling to trigger hydrogel formation (Fig. 1a). Notably, the visual appearance of GA–Zn hydrogels remained essentially unchanged upon the addition of 10 mM $Zn^{2+}$, retaining their transparent supramolecular gel nature, while the incorporation of Rh imparted a uniform yellow color to the system (Fig. 1b). Furthermore, the morphology of GA–Zn–Rh hydrogels was systematically characterized by Cryo-SEM and AFM. Pure GA hydrogels exhibited a uniform, interconnected fibrillar network, forming a micron-scale porous gel network with pore size around 5 μm, whereas the incorporation of 10 mM $Zn^{2+}$ induced a pronounced irregularity and aggregation within the network structure (Fig. S1d and e†). In contrast, $Rh_1$ displayed irregular lamellar and columnar morphologies (Fig. S1f†), which is attributed to the preferential assembly of protonated Rh molecules into globular aggregates in aqueous solution, which further clustered into lamellar and columnar structures, thereby hindering the formation of a continuous three-dimensional network and resulting in a liquid state for $Rh_1$.[36] Intriguingly, in the GA–$Rh_1$, a distinct double network structure was clearly observed, wherein a secondary fibrillar network with submicron-scale gel pore size (approximately 500 nm) was interwoven within the primary GA nanofibrillar network. Notably, these finer fibrils exhibited Rh-derived nano-aggregates adhered to their surfaces (Fig. 1f and g), suggesting a cooperative co-assembly process between GA and Rh. For this hierarchical architecture, GA nanofibrils independently self-assemble to form a primary gel network with ~5 μm pore, while GA–Rh interactions yield a secondary fibrillar gel network of finer dimensions (~500 nm). Upon the addition of $Zn^{2+}$, the double network structure underwent significant aggregation and fusion, characterized by increased pore wall thickness and enlarged pore diameters. This structural evolution is predominantly ascribed to the electrostatic screening effect introduced by $Zn^{2+}$, which modulates the inter-fibrillar interactions and enhances the overall aggregation tendency of the supramolecular system (Fig. 1h). The nanoscale architectures of the hydrogels were further elucidated by AFM. GA alone formed an interconnected three-dimensional fibrillar network through extensive inter-nanofibril entanglements and associations. Notably, the incorporation of $Zn^{2+}$ did not markedly alter the fundamental assembly mode of the GA fibrils but reinforced inter-fibrillar associations, resulting in a denser and more compact network arrangement (Fig. S1a and b†). In contrast, Rh exhibited irregular, polydisperse structures of uneven dimensions, consistent with the morphologies observed in Cryo-SEM (Fig. S1c†). For the GA–$Rh_1$, a distinctive hierarchical structure was evident, where the primary GA fibrillar network intertwined with a secondary GA–Rh co-assembled network, forming an interpenetrating nanofibrillar architecture throughout the matrix (Fig. 1c). Following the introduction of $Zn^{2+}$, the aggregation level within the GA–Zn–$Rh_1$ was markedly enhanced, accompanied by increased pore wall thickness, enlarged pore diameters, and progressive fusion of the double network structure (Fig. 1d and e). These observations are in good agreement with the Cryo-SEM findings (Fig. 1h), confirming the electrostatically mediated modulation of supramolecular assembly behavior by $Zn^{2+}$.

To further elucidate the correlation between nanostructural organization and macroscopic mechanical properties, rheological measurements were performed on the hydrogel systems (Fig. 2). Frequency sweep tests revealed that the incorporation of Rh substantially enhanced both the storage modulus ($G'$) and loss modulus ($G''$) of the GA by nearly an order of magnitude, demonstrating the mechanical reinforcement by the formation of a double nanofibrillar network structure. This significant enhancement reflects the synergistic interplay

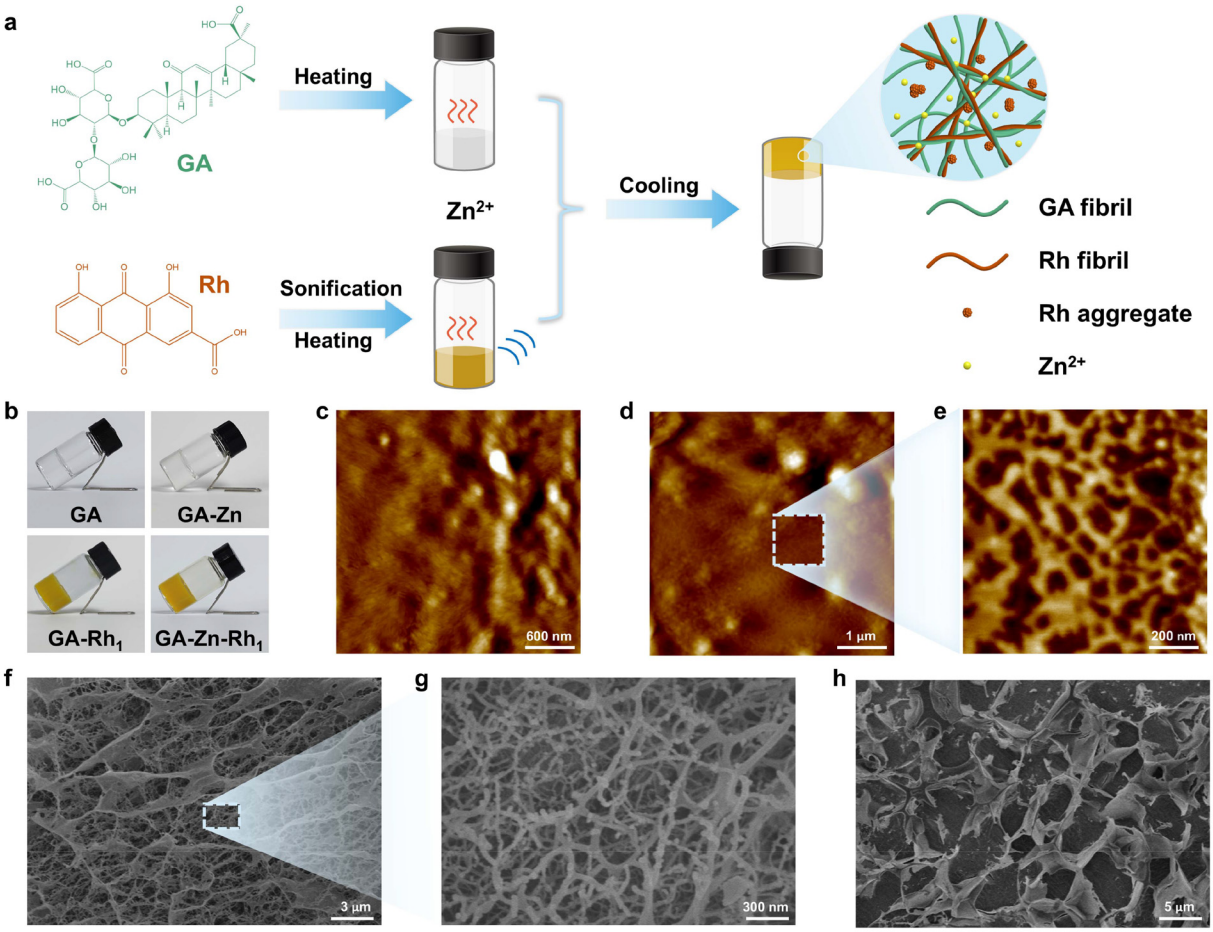


**Fig. 1** (a) Schematic diagram of the fabrication process and (b) digital photos of GA–Zn–Rh hydrogels. AFM height images of (c) GA–$Rh_1$ and (d and e) GA–Zn–$Rh_1$. (e) Magnified image of selected area in image (d). Cryo-SEM images of (f and g) GA–$Rh_1$ and (h) GA–Zn–$Rh_1$. (g) Magnified image of selected area in image (f).

between GA nanofibrils and GA–Rh co-assembled nanostructures within the hierarchical network. More strikingly, the incorporation of $Zn^{2+}$ further amplified the viscoelastic moduli, with the $G'$ of GA–Zn increasing from approximately 50 Pa to nearly 10 000 Pa (Fig. 2a), which is an indicator of stronger fibrillar aggregation and strengthened inter-fibril interactions driven by $Zn^{2+}$-mediated electrostatic screening and complexation effects. Among all tested systems, GA–Zn–$Rh_1$ exhibited the highest viscoelastic moduli, with both $G'$ and $G''$ remaining essentially frequency-independent across the tested range, reflecting the formation of a highly interconnected gel network with excellent mechanical stability. Strain sweep tests provided complementary insights into the mechanical adaptability of the hydrogels (Fig. 2b–d). $Zn^{2+}$ complexation substantially increased the stiffness of the GA, as evidenced by the increased yield and flow stresses, but the reduced yield strain and flow strain mean the increased brittleness. Interestingly, although the addition of Rh alone decreased the critical strains without significantly affecting stresses, the combined GA–Zn–$Rh_1$ maintained yield and flow strains comparable to GA alone while achieving a remarkable increase in yield and flow stresses. This finding highlights a synergistic enhancement in stiffness without compromising toughness, which is attributed to the hierarchical double network structure with thickened pore walls and moderated fibrillar aggregation (Fig. 1d, e and h). Overall, these rheological results demonstrate the role of nanostructure–functionality relationships within the multicomponent hydrogels. The double nanofibrillar architecture, modulated by GA–Rh co-assembly and further consolidated by $Zn^{2+}$-mediated complexation, endows the system with superior mechanical resilience and structural integrity, which lays a structural foundation for the excellent biofunctional performances of GA–Zn–Rh hydrogels in subsequent antibacterial and anti-inflammatory evaluations.

### 3.2 Assembly mechanism of GA–Zn–Rh hydrogels

Elucidating the intermolecular interactions for GA–Zn–Rh hydrogel formation is a key for understanding their assembly mechanism. Isothermal titration calorimetry (ITC) was employed to quantify the thermodynamic parameters governing the interactions between GA and $Zn^{2+}$, as well as GA and

 

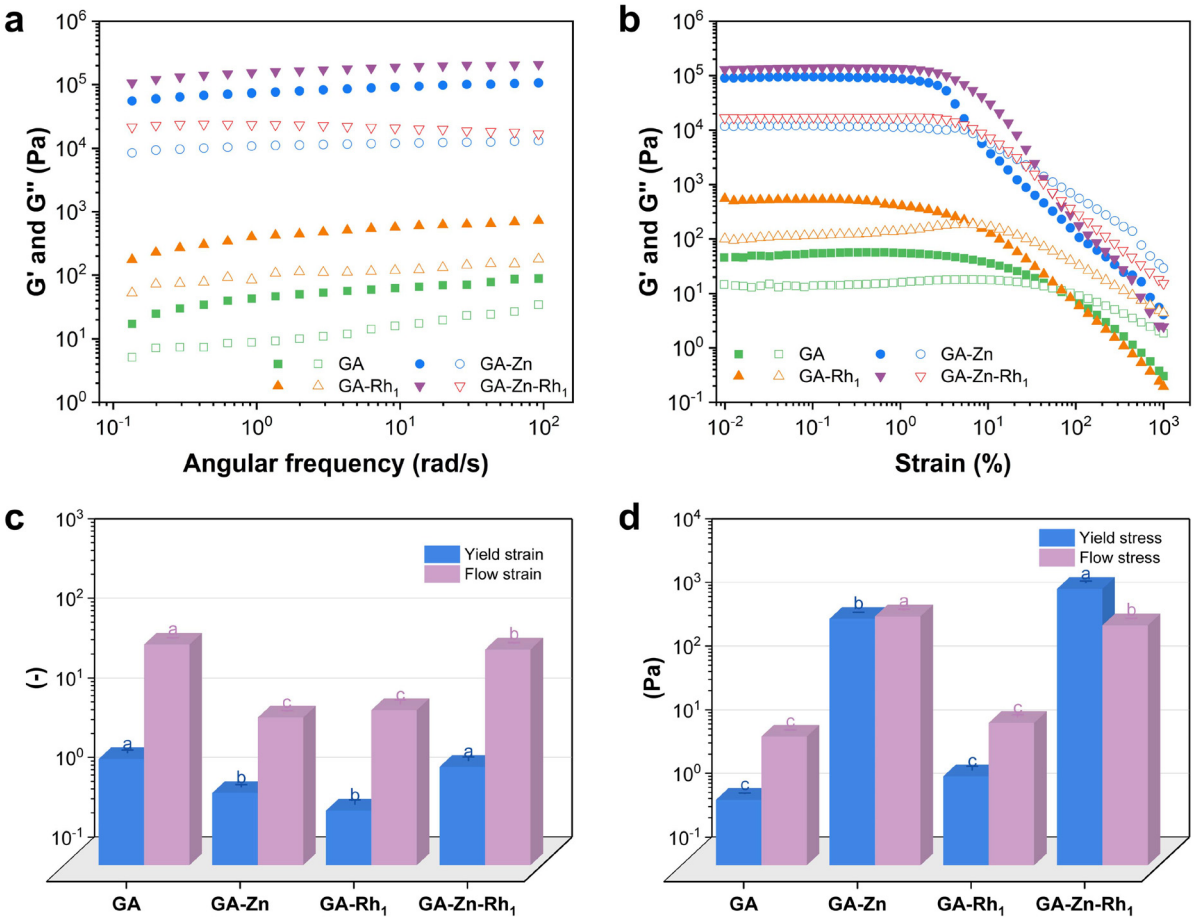


**Fig. 2** (a) Frequency sweeps, (b) strain sweeps, (c) yield and flow strain, and (d) yield and flow stress of GA–Zn–Rh hydrogels. *G′* and *G″* are shown as filled and open symbols, respectively. Different lowercase letters indicate significant differences between samples at the $p < 0.05$ level.

Rh (Fig. 3a and b). The thermodynamic parameters such as binding constant ($K_a$), dissociation constant ($K_d$), Gibbs free energy ($\Delta G$), enthalpy ($\Delta H$) and entropy ($\Delta S$) were obtained by fitting calculation. The $K_a$ values for GA–$Zn^{2+}$ and GA–Rh interactions were determined to be $1.16 \times 10^4$ $M^{-1}$ and $6.80 \times 10^3$ $M^{-1}$, respectively, indicating a strong affinity between GA and $Zn^{2+}$, characteristic of high-affinity binding systems (>$10^4$ $M^{-1}$).[37] The slightly lower binding affinity in the GA–Rh system is attributed to its acidic environment, wherein the limited solubility of Rh and the mutual electrostatic repulsion between negatively charged GA and Rh molecules weaken the interaction strength. The $\Delta G$ values for both GA–$Zn^{2+}$ (−23.21 kJ $mol^{-1}$) and GA–Rh (−21.90 kJ $mol^{-1}$) interactions were negative, confirming the spontaneous nature of these bindings (Fig. 3c).[38] Thermodynamic signatures of $\Delta H < 0$, $\Delta S > 0$, and $|\Delta H| > |T\Delta S|$ for both systems revealed that the interactions were predominantly enthalpy-driven, with electrostatic interactions and hydrogen bonding proposed as the primary driving forces.[39,40]

The intermolecular interactions within the GA–Zn–Rh hydrogels were further elucidated through zeta potential measurements and complementary spectroscopic analyses. Zeta potential data revealed that both GA and Rh individually exhibited negative surface charges of −35.7 mV and −30.0 mV, respectively. Upon co-assembly, the GA–Rh system displayed a markedly enhanced negative surface charge of −56.6 mV, which is indicative of strong electrostatic repulsion between the components. However, the introduction of $Zn^{2+}$ substantially reduced this negative charge, with the zeta potential of the GA–Zn–Rh hydrogel increasing to −31.7 mV, meaning a pronounced electrostatic screening effect mediated by the complexed metal ions (Fig. 3d). The molecular interactions underlying the hydrogel assembly were further elucidated by FTIR of the lyophilized hydrogel samples (Fig. 3e). For GA, the characteristic absorption bands were observed at 1726 $cm^{-1}$ (C=O stretching vibration), 1657 $cm^{-1}$ (C=C stretching vibration in the triterpene skeleton), 1398 $cm^{-1}$ (C–H bending vibration of $-CH_3$ group), 1215 $cm^{-1}$ (C–O stretching vibration) and 1172 $cm^{-1}$ (C–O–C stretching vibration within diglucuronic unit).[34,41] The introduction of 10 mM $Zn^{2+}$ did not produce significant shifts in the characteristic peaks of GA–Zn, in agreement with earlier findings.[34] For $Rh_1$, the characteristic peaks mainly appeared near 3062 $cm^{-1}$ (C–H stretching vibration of benzene ring), 1693 $cm^{-1}$ (C=O stretching

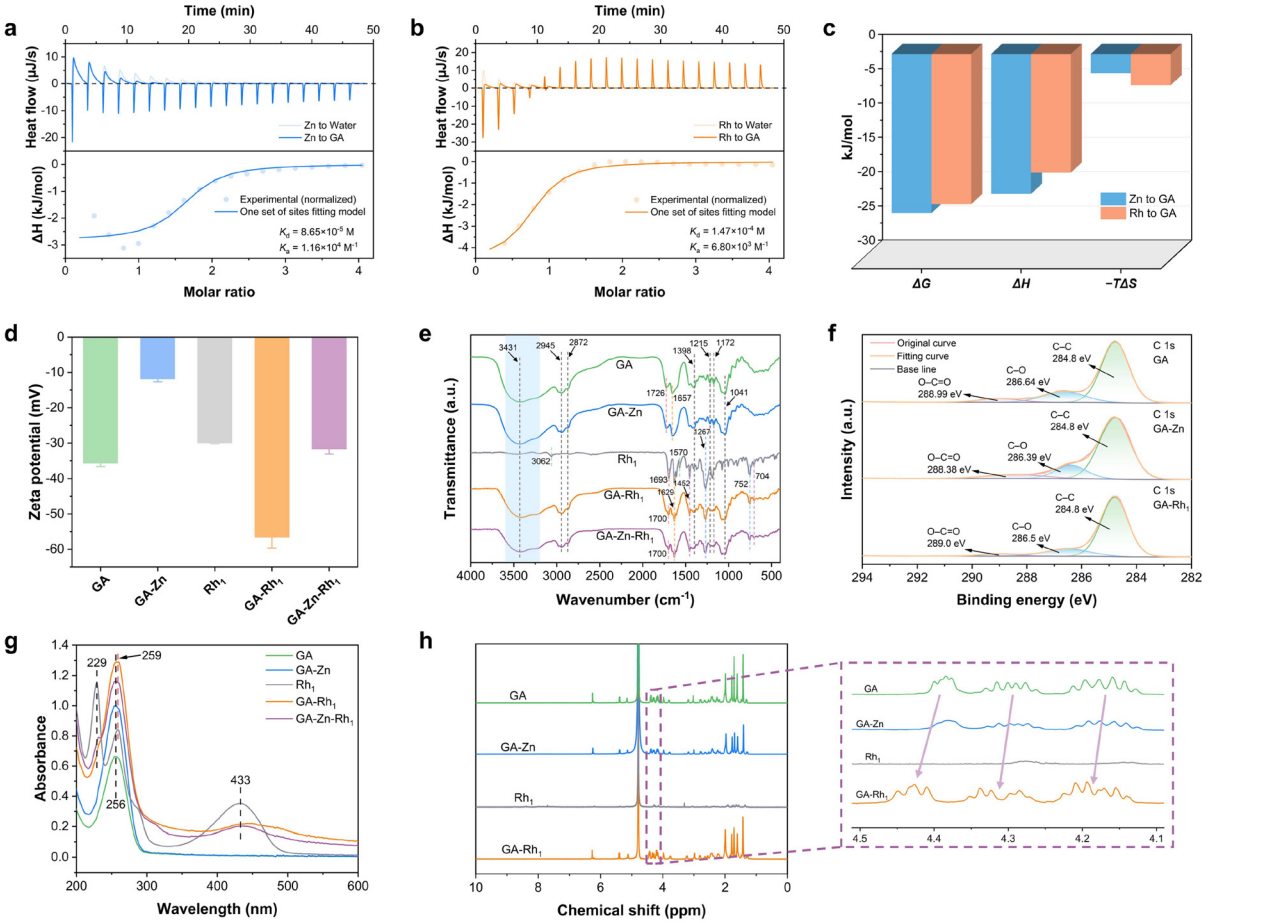


**Fig. 3** Assembly mechanism of GA–Zn–Rh hydrogels. ITC raw heat flow and fitting curves for the interaction of (a) $Zn^{2+}$ with GA and (b) Rh with GA. (c) Thermodynamic parameters ($\Delta G$, $\Delta H$, and $-T\Delta S$) for the binding of $Zn^{2+}$ to GA and Rh to GA. (d) Zeta potential, (e) FTIR spectra, (f) high-resolution XPS C 1s spectra, (g) UV-Vis spectra, and (h) $^1$H-NMR of GA–Zn–Rh hydrogels.

vibration of ketone), 1570 cm$^{-1}$ (C=C stretching vibration of aromatic ring), 1452 cm$^{-1}$ (C–O stretching vibration of carboxyl group), 1267 cm$^{-1}$ (O–H bending vibration) and 752 cm$^{-1}$ (meso-substitution of benzene).[42,43] Upon co-assembly within GA–Rh$_1$ and GA–Zn–Rh$_1$, marked spectral changes were observed. As can be seen, the C–H stretching band of the Rh aromatic ring and the C=O stretching band of GA diminished, while the C=O stretching band of the Rh ketone shifted to 1700 cm$^{-1}$. Simultaneously, the C=C stretching bands corresponding to both the GA triterpenoid skeleton and Rh aromatic ring disappeared. Notably, the intensities of the C–O stretching and O–H bending vibrations associated with the Rh carboxyl group, as well as the C–H bending, C–O stretching, and C–O–C stretching vibrations within GA, were diminished. Additionally, the meso-substitution band of the Rh benzene ring was weakened. These spectral changes collectively suggest that the co-assembly between GA and Rh is primarily driven by hydrogen bonding, hydrophobic interactions among the hydrophobic backbones, and electrostatic interactions involving carboxylate groups. Importantly, the incorporation of $Zn^{2+}$ did not induce substantial alterations in the molecular frameworks of either GA or Rh.

These interaction mechanisms were further confirmed by XPS analysis. As shown in the high-resolution C 1s spectra, the intensities of the C–O and O=C–O groups decreased in both GA–Zn and GA–Rh$_1$, while there is no significant change in the position of the binding energies of the groups (Fig. 3f). Complementary UV-Vis absorption spectroscopy revealed a characteristic C=C absorption peak at 256 nm for GA, which remained essentially unchanged upon the addition of $Zn^{2+}$ (Fig. 3g). In contrast, Rh$_1$ exhibited distinct anthraquinone-associated absorption bands at 229, 259, and 433 nm. Notably, in both GA–Zn and GA–Rh$_1$, the absorption band at 229 nm disappeared, while the 433 nm peak underwent a red shift, suggesting π–π stacking interactions between Rh molecules and between GA and Rh, resulting in the formation of J-aggregates.[31,44] Further evidence for intermolecular hydrogen bonding between GA and Rh was obtained from $^1$H NMR spectroscopy. Upon complexation, the proton signals corresponding to the diglucuronic acid moiety of GA exhibited both

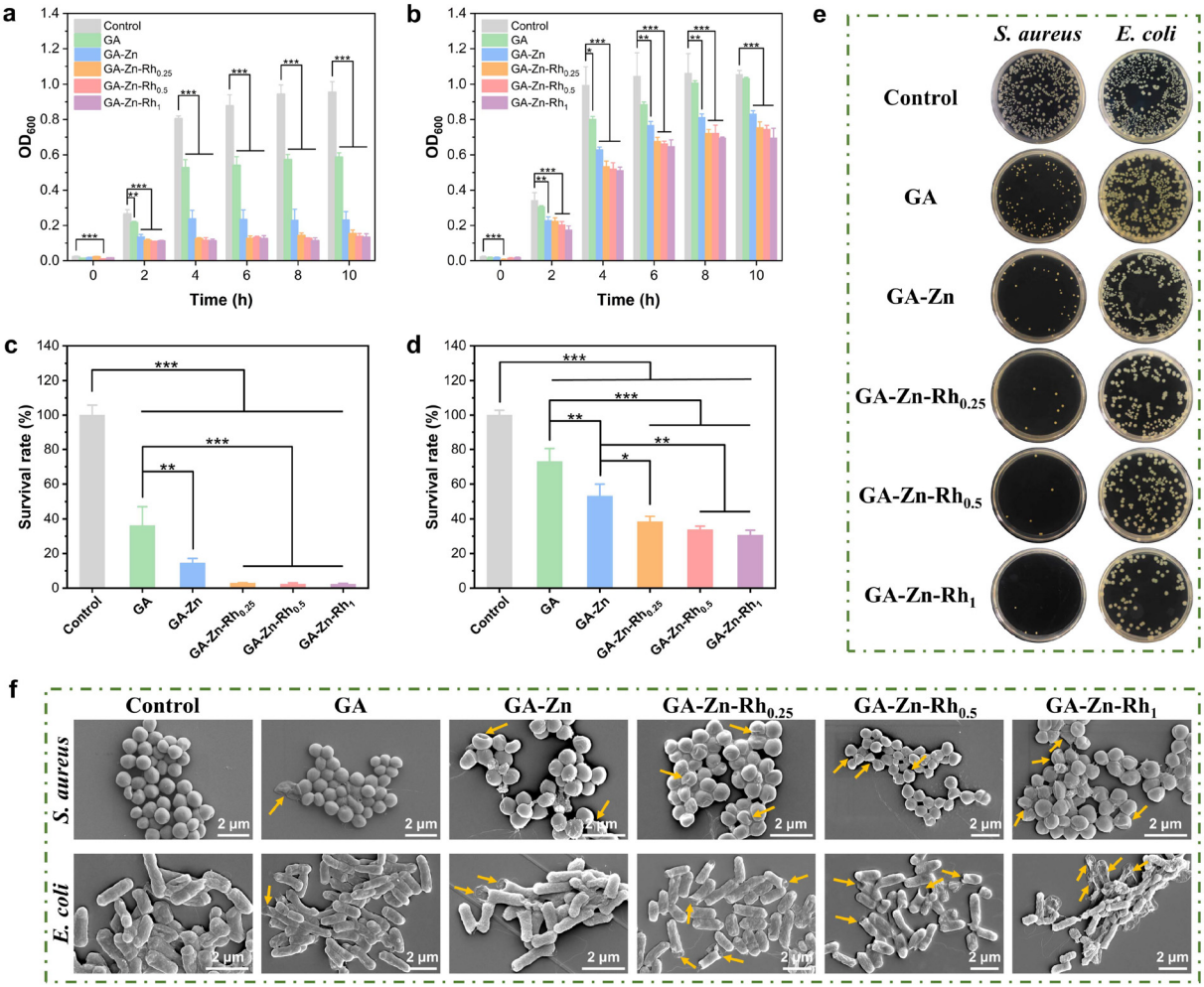


**Fig. 4** Antibacterial properties of GA–Zn–Rh hydrogels. Optical density ($OD_{600}$) growth curves of (a) *S. aureus* and (b) *E. coli* incubating with GA–Zn–Rh hydrogels. Survival rates of (c) *S. aureus* and (d) *E. coli* after treatment with GA–Zn–Rh hydrogels. (e) Photographs of bacterial agar plates after incubation with GA–Zn–Rh hydrogels. (f) FE-SEM images of *S. aureus* and *E. coli* after treatment with GA–Zn–Rh hydrogels (*$p < 0.05$, **$p < 0.01$, ***$p < 0.001$).

a downfield shift and peak shape changes, reflecting the formation of hydrogen bonds and alterations in the local chemical environment (Fig. 3h). Collectively, these results confirm that the GA–Zn–Rh hydrogel network is primarily stabilized by a combination of non-covalent interactions, including GA–GA inter-fibrillar hydrogen bonding, complexation between GA and $Zn^{2+}$, and a synergistic interplay of intermolecular hydrogen bonding, hydrophobic interactions, electrostatic forces, and π–π stacking between GA and Rh.

### 3.3 *In vitro* antibacterial properties

The antibacterial performance of the GA–Zn–Rh hydrogels was assessed against *Staphylococcus aureus* (*S. aureus*, Gram-positive bacteria) and *Escherichia coli* (*E. coli*, Gram-negative bacteria). Additionally, the influence of Rh concentration on the antibacterial efficacy of the hydrogels was also investigated. As shown in the bacterial growth curves ($OD_{600}$) for *S. aureus*, GA alone exhibited moderate antibacterial activity relative to the PBS control, which was promoted upon incorporation of $Zn^{2+}$. Notably, the introduction of Rh into the GA–Zn system markedly enhanced the inhibitory effect, with GA–Zn–$Rh_x$ effectively suppressing bacterial growth, maintaining $OD_{600}$ values around 0.1 from 2 to 10 h. Furthermore, the antibacterial capacity was positively correlated with the increasing Rh concentration (Fig. 4a). Compared with *S. aureus*, GA exhibited minimal inhibitory activity against *E. coli*, with $OD_{600}$ values showing no significant difference from the control group after 8 h of incubation. However, the incorporation of $Zn^{2+}$ substantially improved the antibacterial performance, and this effect was further amplified in the GA–Zn–$Rh_x$. Notably, increasing the concentration of Rh consistently enhanced the antibacterial efficacy against *E. coli* (Fig. 4b). To further verify these findings, quantitative antibacterial assays were performed *via* plate counting. As illustrated in Fig. 4c, *S. aureus* exhibited a survival rate of 36.2% after treatment with GA, which was decreased markedly to 14.4% upon the addition of $Zn^{2+}$. Strikingly, the

GA–Zn–Rh$_x$, particularly at higher Rh concentrations, demonstrated near-complete bactericidal activity, with survival rates approaching zero (Fig. 4c and e). A comparable trend was observed for *E. coli* (Fig. 4d), where the survival rate after exposure to GA remained at 73.0%, reducing to 53.1% following $Zn^{2+}$ incorporation. Further, the survival rate progressively decreased from 38.3% to 30.6% as the Rh concentration increased in GA–Zn–Rh$_x$ (Fig. 4d and e). These results confirm the synergistic antibacterial effect of $Zn^{2+}$ and Rh within the GA-based hydrogel system. Further morphological evidence of the antibacterial mechanism was obtained *via* FE-SEM. As depicted in Fig. 4f, the untreated *S. aureus* and *E. coli* exhibited smooth and intact surfaces, whereas bacteria exposed to GA–Zn–Rh hydrogels displayed pronounced membrane shrinkage, surface wrinkling, and cellular rupture (indicated by arrows), with these effects being the most evident in the GA–Zn–Rh$_x$ groups. These morphological alterations directly correlate with the observed antibacterial performance. The antibacterial activity of the GA–Zn–Rh hydrogels can be primarily attributed to the intrinsic bioactivities of their constituent components—GA, Rh, and $Zn^{2+}$—each of which can disrupt bacterial membrane integrity and interfere with essential intracellular processes, including the synthesis of bacterial DNA, RNA, and proteins.[45,46] In addition to the chemical bioactivity of these molecules, growing evidence indicates that the three-dimensional structural features of supramolecular nano-assemblies—such as their shape, size, surface area, and hierarchical organization—significantly influence their biological behavior and therapeutic efficacy by modulating interfacial interactions, for example through the formation of a protein corona (biocorona).[47,48] In our work, the hierarchical nanofibrillar networks constructed by GA nanofibrils and GA–Rh co-assemblies, further regulated by $Zn^{2+}$ complexation, exhibit distinct morphologies and multiscale dimensional characteristics. These features are presumed to enhance the diffusion of bioactive components, promote intimate interactions with bacterial membranes, and collectively contribute to the superior antibacterial performance of the GA–Zn–Rh hydrogel system, thereby underscoring the pivotal role of nanostructure–function relationships in modulating the bioactivity of multicomponent hydrogels derived from natural herbal small molecules. Notably, the inhibitory effect of GA–Zn–Rh hydrogels against *E. coli* was markedly lower than that against *S. aureus*, which can be explained by the fundamental structural differences between Gram-positive and Gram-negative bacterial cell envelopes. Compared to Gram-positive bacteria such as *S. aureus*, Gram-negative bacteria like *E. coli* possess a dual-layered cell wall structure, comprising an outer lipopolysaccharide membrane and an inner phospholipid membrane. The dense, negatively charged lipopolysaccharide layer functions as a robust permeability barrier, impeding the penetration of the negatively charged GA–Zn–Rh hydrogels and consequently reducing

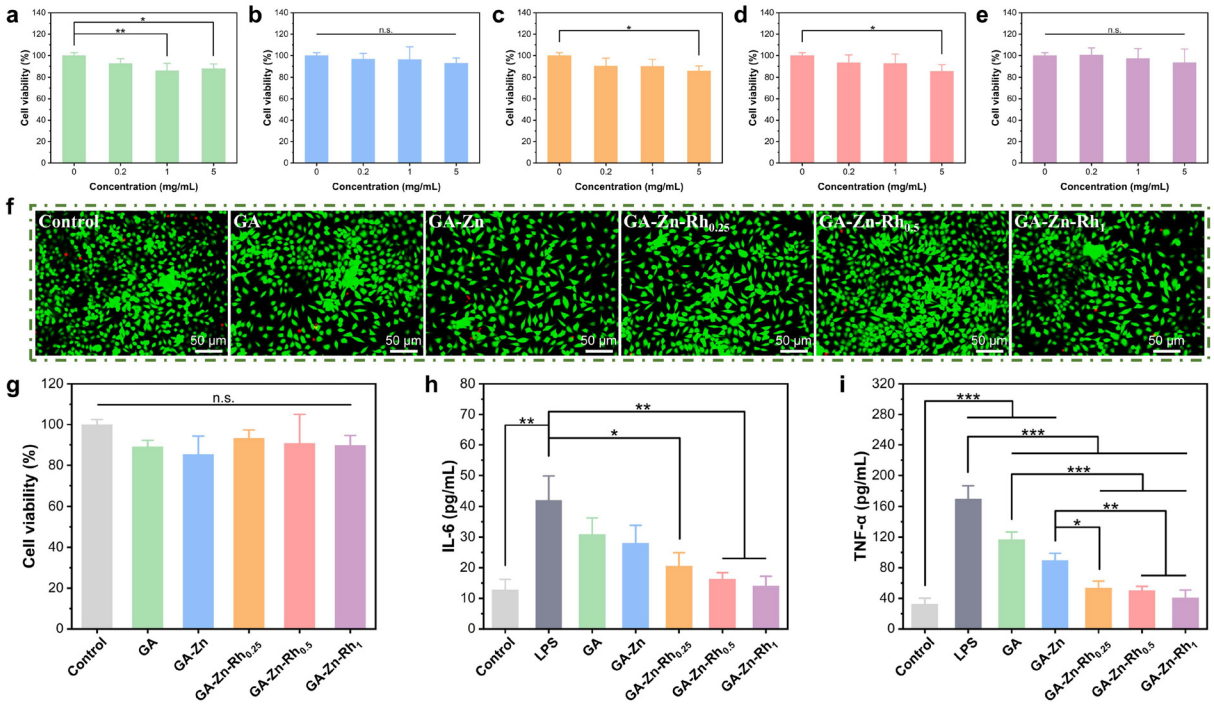


**Fig. 5** *In vitro* biocompatibility and anti-inflammation ability of GA–Zn–Rh hydrogels. (a–e) Viability of L929 cells incubated with GA–Zn–Rh hydrogel extract liquids at different concentrations (0, 0.2, 1, and 5 mg mL$^{-1}$) for 24 h by MTT assay: (a) GA, (b) GA–Zn, (c) GA–Zn–R$_{0.25}$, (d) GA–Zn–R$_{0.5}$, and (e) GA–Zn–R$_1$. (f) Live/dead fluorescence staining images of L929 cells incubated with hydrogel extract liquids (5 mg mL$^{-1}$) for 24 h. (g) Viability of RAW264.7 cells incubated with GA–Zn–Rh hydrogel extract liquids at 5 mg mL$^{-1}$ for 24 h by MTT assay. Intracellular (h) IL-6 and (i) TNF-α levels in LPS-stimulated RAW246.7 cells after treatment with GA–Zn–Rh hydrogel extract liquids at 5 mg mL$^{-1}$ for 24 h (*$p$ < 0.05, **$p$ < 0.01, ***$p$ < 0.001).

their antibacterial efficacy against *E. coli*.[49,50] Taken together, these results demonstrate that compared to GA alone, the GA–Zn–Rh hydrogels possess potent antibacterial activity, effectively suppressing the growth and proliferation of *S. aureus*, and also exhibiting significantly enhanced inhibitory effects against *E. coli*.

### 3.4 *In vitro* biocompatibility and anti-inflammation effects

As a promising antibacterial and anti-inflammatory biomaterial, the biocompatibility of GA–Zn–Rh hydrogels is a critical prerequisite for their potential biomedical applications. Therefore, the cytocompatibility of GA, GA–Zn, and GA–Zn–$Rh_x$ was systematically evaluated using MTT assays against L929 fibroblasts and RAW264.7 macrophages. As shown in Fig. 5a–e and Fig. S3a–e,† the average cell viability of both L929 and RAW264.7 cells remained above 85% after 24 h incubation with extract liquids of GA, GA–Zn, and GA–Zn–$Rh_x$ at various concentrations, indicating that these hydrogels exerted negligible cytotoxic effects within the tested concentration range. To further visualize cellular viability and morphology, live/dead fluorescence staining was performed. Live cells emitted green fluorescence, while dead cells exhibited red fluorescence. After 24 h of co-culture with 5 mg $mL^{-1}$ extract liquids of GA, GA–Zn, and GA–Zn–$Rh_x$, both L929 and RAW264.7 cells displayed normal, healthy morphology—spindle-shaped for L929 fibroblasts and round-shaped for RAW264.7 macrophages, which are comparable to those of the control group, with scarcely any dead cells detected (Fig. 5f and Fig. S3f†). The above results demonstrate that GA–Zn–Rh hydrogels possess excellent cytocompatibility and exhibit no appreciable cytotoxicity towards both fibroblasts and macrophages under the tested conditions, which demonstrate their suitability for biomedical applications involving antibacterial and anti-inflammatory therapies.

An efficient anti-inflammatory capability is essential for hydrogels intended for wound healing applications to mitigate excessive inflammatory responses. To evaluate this property, RAW264.7 macrophages were stimulated with lipopolysaccharide (LPS) to induce a pro-inflammatory M1 phenotype, characterized by the upregulation of pro-inflammatory cytokines. After co-incubation with extract liquids of GA, GA–Zn, and GA–Zn–$Rh_x$ (5 mg $mL^{-1}$) for 24 h, the average viability of RAW264.7 cells remained above 85% (Fig. 5g), confirming that this *in vitro* model is appropriate for anti-inflammatory assessment. IL-6 and TNF-α are key pro-inflammatory cytokines involved in the inflammatory cascade,[51] and their levels were subsequently measured to evaluate the anti-inflammatory efficacy of the hydrogels. As shown in Fig. 5h and i, LPS stimulation markedly elevated the secretion of both IL-6 and TNF-α compared to the unstimulated control group, indicating the successful establishment of an inflammation model. Notably, treatment with GA–Zn–$Rh_x$ extract liquids for 24 h significantly suppressed IL-6 production, with levels decreasing from 20.48 pg $mL^{-1}$ to 13.99 pg $mL^{-1}$ as the Rh concentration increased, approaching that of the control group (12.77 pg $mL^{-1}$) (Fig. 5h). Similarly, TNF-α secretion was substantially reduced from 53.36 pg $mL^{-1}$ to 40.54 pg $mL^{-1}$ with increasing Rh concentrations, also near the baseline level of the control group (32.43 pg $mL^{-1}$) (Fig. 5i). These *in vitro* findings demonstrate that GA–Zn–Rh hydrogels possess pronounced anti-inflammatory properties, mainly due to the synergistic bioactivity of the naturally derived GA and Rh molecules, which effectively suppress the production of inflammatory cytokines and thereby modulate macrophage-mediated inflammatory responses.[28,31,52,53] Additionally, this anti-inflammatory performance is closely associated with the hierarchical double nanofibrillar nanostructures within the hydrogels, as the distinct nano-architectures influence the interactions between the hydrogel assemblies and immune cells, further regulating inflammatory signaling pathways and enhancing biofunctional outcomes.[54]

## 4 Conclusions

In summary, we successfully developed GA–Zn–Rh co-assembled bioactive supramolecular hydrogels by modulating the self-assembly behavior of two natural LMWGs, GA and Rh, *via* $Zn^{2+}$ complexation. These hydrogels were predominantly stabilized through a combination of non-covalent interactions, including GA–GA hydrogen bonding, GA–$Zn^{2+}$ complexation, and intermolecular hydrogen bonding, hydrophobic, electrostatic forces, and π–π stacking between GA and Rh. Notably, a hierarchical nanofibrillar network structure was formed, wherein GA nanofibrils self-assembled to form a primary gel network featuring micron-scale pore sizes (~5 μm), while a secondary, denser gel network with submicron-scale pore sizes (~500 nm) emerged through the co-assembly of GA and Rh. Importantly, the introduction of $Zn^{2+}$ not only regulated the assembly dynamics by electrostatic screening effects but also enhanced the double network architecture by increasing pore wall thickness, enlarging pore diameters, and promoting fibrillar aggregation and fusion. These nanostructural features profoundly influenced the mechanical properties and biological functions of the hydrogels. Co-assembly with Rh significantly improved the viscoelastic moduli, while $Zn^{2+}$ further strengthened network connectivity, enhancing stiffness without sacrificing toughness. Biologically, the GA–Zn–Rh hydrogels demonstrated potent antibacterial activity (especially against *S. aureus*) and exhibited excellent biocompatibility alongside remarkable anti-inflammatory effects, primarily attributed to the synergistic bioactivities of GA, Rh, and $Zn^{2+}$ and the functional advantages imparted by the hierarchical fibrillar nanostructure. This work not only elucidates the critical nanostructure–functionality relationships governing the performance of multicomponent supramolecular hydrogels assembled from natural herbal-derived LMWGs but also offers a supramolecular-level design strategy to emulate the synergistic therapeutic principles of traditional herbal medicine. These findings offer useful insights for the rational design of nature-inspired bioactive hydrogels for biomedical applications. Nonetheless, challenges such as long-term stability, *in vivo* performance, and scalable fabrication remain to be addressed in

future studies to fully realize the clinical potential of these biomaterials.

## Author contributions

Xinke Yu: investigation, methodology, formal analysis, visualization, writing – original draft. Sili Liu: investigation, methodology. Zhili Wan: conceptualization, methodology, supervision, project administration, funding acquisition, resources, formal analysis, writing – review & editing. Xiaoquan Yang: conceptualization, resources.

## Conflicts of interest

There are no conflicts to declare.

## Data availability

The data are available upon reasonable request.

## Acknowledgements

This work is financially supported by the Outstanding Youth Project of Guangdong Natural Science Foundation (2024B1515020081), the National Natural Science Foundation of China (32172347), and the 111 Project (B17018).

## References

1 L. E. Buerkle and S. J. Rowan, *Chem. Soc. Rev.*, 2012, **41**, 6089.
2 X. Du, J. Zhou, J. Shi and B. Xu, *Chem. Rev.*, 2015, **115**, 13165–13307.
3 E. R. Draper and D. J. Adams, *Chem*, 2017, **3**, 390–410.
4 P. R. A. Chivers and D. K. Smith, *Nat. Rev. Mater.*, 2019, **4**, 463–478.
5 D. J. Adams, *J. Am. Chem. Soc.*, 2022, **144**, 11047–11053.
6 D. K. Smith, *Soft Matter*, 2024, **20**, 10–70.
7 K. Zhi, H. Zhao, X. Yang, H. Zhang, J. Wang, J. Wang and J. M. Regenstein, *Nanoscale*, 2018, **10**, 3639–3643.
8 H. Huang, W. Gong, X. Wang, W. He, Y. Hou and J. Hu, *Adv. Healthcare Mater.*, 2022, **11**, 2102476.
9 M. Hao, S. Wei, S. Su, Z. Tang and Y. Wang, *ACS Appl. Mater. Interfaces*, 2024, **16**, 24221–24234.
10 X. Guo, W. Luo, L. Wu, L. Zhang, Y. Chen, T. Li, H. Li, W. Zhang, Y. Liu, J. Zheng and Y. Wang, *Adv. Sci.*, 2024, **11**, 2403388.
11 M. Peng, Q. Peng, W. Li, X. Chen, Q. Yan, X. Wu, M. Wu, D. Yuan, H. Song and J. Shi, *Adv. Mater.*, 2025, **37**, 2503283.
12 M. Li, H. Wang, J. Hu, J. Hu, S. Zhang, Z. Yang, Y. Li and Y. Cheng, *Chem. Mater.*, 2019, **31**, 7678–7685.
13 Z. Wang, J. Lu, Z. Yuan, W. Pi, X. Huang, X. Lin, Y. Zhang, H. Lei and P. Wang, *Small*, 2023, **19**, 2205528.
14 S. Fu and X. Yang, *J. Mater. Chem. B*, 2023, **11**, 4584–4599.
15 Y. Ji, Y. Yuan, F. Peng, S. Fu, B. Liu, Z. Dong, Q. Li, S. Ma and Z. Ao, *ACS Appl. Mater. Interfaces*, 2025, **17**, 5223–5231.
16 W. Luo, Z. Yang, J. Zheng, Z. Cai, X. Li, J. Liu, X. Guo, M. Luo, X. Fan, M. Cheng, T. Tang, J. Liu and Y. Wang, *ACS Nano*, 2024, **18**, 28894–28909.
17 C. Lei, J. Wen, Y. Sun, M. Ren, R. Qiao and C. Li, *Chem. Eng. J.*, 2025, **503**, 158477.
18 M. N. Asl and H. Hosseinzadeh, *Phytother. Res.*, 2008, **22**, 709–724.
19 B. Schröfelbauer, J. Raffetseder, M. Hauner, A. Wolkerstorfer, W. Ernst and O. H. J. Szolar, *Biochem. J.*, 2009, **421**, 473–482.
20 Z. Zhao, Y. Xiao, L. Xu, Y. Liu, G. Jiang, W. Wang, B. Li, T. Zhu, Q. Tan, L. Tang, H. Zhou, X. Huang and H. Shan, *ACS Appl. Mater. Interfaces*, 2021, **13**, 20995–21006.
21 Q. Li, M. Xu, J. Xie, E. Su, Z. Wan, L. M. C. Sagis and X. Yang, *Food Res. Int.*, 2021, **140**, 110076.
22 Q. Li, Z. Wan and X. Yang, *Curr. Opin. Food Sci.*, 2022, **43**, 107–113.
23 A. Saha, J. Adamcik, S. Bolisetty, S. Handschin and R. Mezzenga, *Angew. Chem., Int. Ed.*, 2015, **54**, 5408–5412.
24 X. Yu, Y. Meng, H. Zhang, J. Guo, S. Wang, H. Li, J. Hu and M. H. Li, *Nanoscale*, 2021, **13**, 15257–15266.
25 L. Zhao, H. Zhang, Z. Guo, X. Yu, X. Jiao, M. H. Li and J. Hu, *ACS Appl. Mater. Interfaces*, 2022, **14**, 51394–51403.
26 W. Liu, Z. Li, Z. Wang, Z. Huang, C. Sun, S. Liu, Y. Jiang and H. Yang, *ACS Appl. Mater. Interfaces*, 2023, **15**, 7767–7776.
27 Q. Li, X. Yu, S. Zhang, M. Xu, Y. Yang, Z. Wan and X. Yang, *ACS Appl. Mater. Interfaces*, 2023, **15**, 43633–43647.
28 Q. Li, S. Zhang, R. Du, Y. Yang, Y. Liu, Z. Wan and X. Yang, *ACS Appl. Mater. Interfaces*, 2023, **15**, 17562–17576.
29 X. Yu, J. Cai, M. Xu, Q. Li, Y. Yang, Z. Wan and X. Yang, *Nanoscale*, 2024, **16**, 14261–14268.
30 Q. Li, Y. Liu, S. Liu, S. Zhang, X. Yu, Z. Wan, Y. Yuan, P. V. der Meeren and X. Yang, *Chem. Eng. J.*, 2025, **512**, 162677.
31 J. Zheng, R. Fan, H. Wu, H. Yao, Y. Yan, J. Liu, L. Ran, Z. Sun, L. Yi, L. Dang, P. Gan, P. Zheng, T. Yang, Y. Zhang, T. Tang and Y. Wang, *Nat. Commun.*, 2019, **10**, 1604.
32 W. Fu, M. Guo, X. Zhou, Z. Wang, J. Sun, Y. An, T. Guan, M. Hu, J. Li, Z. Chen, J. Ye, X. Gao, G. F. Gao, L. Dai, Y. Wang and C. Chen, *ACS Nano*, 2024, **18**, 11200–11216.
33 D. Zhong, K. Jin, R. Wang, B. Chen, J. Zhang, C. Ren, X. Chen, J. Lu and M. Zhou, *Adv. Mater.*, 2024, **36**, 2312275.
34 X. Yu, M. Xu, J. Cai, Q. Li, Y. Yang, Z. Wan and X. Yang, *Giant*, 2024, **17**, 100240.
35 K. Wong, Z. Nie, M. Wong, Y. Wang and J. Liu, *Adv. Mater.*, 2024, **36**, 2404053.
36 Y. H. Feng, X. P. Zhang, Y. Y. Hao, G. Y. Ren and X. D. Guo, *Colloids Surf., B*, 2020, **195**, 111260.
37 W. B. Turnbull and A. H. Daranas, *J. Am. Chem. Soc.*, 2003, **125**, 14859–14866.
38 W. Pi, L. Wu, J. Lu, X. Lin, X. Huang, Z. Wang, Z. Yuan, H. Qiu, J. Zhang, H. Lei and P. Wang, *Bioact. Mater.*, 2023, **29**, 98–115.

39 A. R. Patel, J. Seijen-ten-Hoorn, P. C. M. Heussen, E. Drost, J. Hazekamp and K. P. Velikov, *J. Colloid Interface Sci.*, 2012, **374**, 150–156.
40 P. Sarker, P. K. Jani, L. C. Hsiao, O. J. Rojas and S. A. Khan, *J. Colloid Interface Sci.*, 2023, **650**, 541–552.
41 E. Su, Q. Li, M. Xu, Y. Yuan, Z. Wan, X. Yang and B. P. Binks, *J. Colloid Interface Sci.*, 2021, **587**, 797–809.
42 S. Petralito, I. Zanardi, R. Spera, A. Memoli and V. Travagli, *Spectrochim. Acta, Part A*, 2014, **127**, 355–360.
43 C. Yin, X. Han, Q. Lu, X. Qi, C. Guo and X. Wu, *Int. J. Biol. Macromol.*, 2022, **201**, 14–19.
44 D. Cai, Y. Yang, J. Lu, Z. Yuan, Y. Zhang, X. Yang, X. Huang, T. Li, X. Tian, B. Xu, P. Wang and H. Lei, *ACS Appl. Mater. Interfaces*, 2022, **14**, 43035–43049.
45 H. K. Kim, Y. Park, H. N. Kim, B. H. Choi, H. G. Jeong, D. G. Lee and K.-S. Hahm, *Biotechnol. Lett.*, 2002, **24**, 1899–1902.
46 J. Azelmat, J. F. Larente and D. Grenier, *Arch. Oral Biol.*, 2015, **60**, 342–346.
47 C. Ge, J. Du, L. Zhao, L. Wang, Y. Liu, D. Li, Y. Yang, R. Zhou, Y. Zhao, Z. Chai and C. Chen, *Proc. Natl. Acad. Sci. U. S. A.*, 2011, **108**, 16968–16973.
48 P. Zhang, M. Cao, A. J. Chetwynd, K. Faserl, F. A. Monikh, W. Zhang, R. Ramautar, L. J. A. Ellis, H. H. Davoudi, K. Reilly, R. Cai, K. E. Wheeler, D. S. T. Martinez, Z. Guo, C. Chen and I. Lynch, *Nat. Protoc.*, 2024, **19**, 3000–3047.
49 R. Huwaitat, A. P. McCloskey, B. F. Gilmore and G. Laverty, *Future Microbiol.*, 2016, **11**, 955–972.
50 R. Ruhal and R. Kataria, *Microbiol. Res.*, 2021, **251**, 126829.
51 J. Deng, D. Lin, X. Ding, Y. Wang, Y. Hu, H. Shi, L. Chen, B. Chu, L. Lei, C. Wen, J. Wang, Z. Qian and X. Li, *Adv. Funct. Mater.*, 2022, **32**, 2109173.
52 Y. Qian, Y. Zheng, J. Jin, X. Wu, K. Xu, M. Dai, Q. Niu, H. Zheng, X. He and J. Shen, *Adv. Mater.*, 2022, **34**, 2200521.
53 W. Zhao, X. Zhang, R. Zhang, K. Zhang, Y. Li and F.-J. Xu, *ACS Appl. Mater. Interfaces*, 2020, **12**, 56898–56907.
54 Y. Li, R. Yuan, Y. Luo, X. Guo, G. Yang, X. Li and S. Zhou, *Adv. Mater.*, 2023, **35**, 2300216.